Catalysis Today 168 (2011) 71–79

Contents lists available at ScienceDirect

Catalysis Today

journal homepage: www.elsevier.com/locate/cattod

Hierarchical ZSM-5 prepared by guanidinium base treatment: Understanding microstructural characteristics and impact on MTG and NH_3-SCR catalytic reactions

Peter N.R. Vennestrøm[a,b], Marie Grill[a], Marina Kustova[a], Kresten Egeblad[a], Lars F. Lundegaard[a], Finn Joensen[a], Claus H. Christensen[a,1], Pablo Beato[a,*]

[a] Haldor Topsøe A/S, Nymøllevej 55, DK-2800 Lyngby, Denmark
[b] Instituto de Tecnología Química, UPV, Av. Naranjos s/n, E-46022 Valencia, Spain

ARTICLE INFO

Article history:
Received 18 October 2010
Received in revised form 2 February 2011
Accepted 17 March 2011

Keywords:
H-ZSM-5
Hierarchical zeolites
Methanol-to-gasoline
Fe-ZSM-5
Selective catalytic reduction

ABSTRACT

An H-ZSM-5 zeolite sample consisting of large particles (5–15 μm) was synthesized and base treated using sodium hydroxide, guanidinium hydroxide and guanidinium carbonate to create a hierarchical pore system. In the case of sodium hydroxide as demetallation agent a high degree of mesoporosity was achieved and with guanidinium hydroxide, mesoporosity was observed after prolonged treatment. All samples were tested in the methanol-to-gasoline (MTG) reaction and iron-impregnated samples were tested for selective catalytic reduction of NO with ammonia (SCR). In the MTG reaction an improved catalyst lifetime was observed which has been correlated to the creation of mesopores. In the SCR reaction improved NO conversion was observed for all base treated samples. In accordance with spectroscopic results this has been attributed to a higher abundance of active and dispersed Fe sites in the base treated samples. All samples were characterized by a multitude of experimental techniques including physisorption measurements, electron microscopy and spectroscopic methods.

1. Introduction

Zeolites represent an important group of crystalline inorganic materials containing micropores with well-defined structures. They are widely applied in industry for separation, adsorption and catalysis, and may be tailored with respect to different properties such as the number and strength of acid sites, redox properties, the hydrophobicity/hydrophilicity of the micropores and the pore architecture [1–3]. For catalytic applications, the wide range of zeolite structures with different pore sizes and pore geometries entails various kinds of shape selectivity. However, in many cases it appears that the sole presence of micropores in zeolite catalysts may also limit the catalytic performance of the zeolite, particularly when diffusion in the micropores becomes significantly slower than the catalytic reaction. Over the last decade it has been established, that the presence of an auxiliary mesopore system effectively enhances the rate of diffusion of molecules in zeolites [4–7], leading to improved catalytic activity and longer catalyst lifetime [7–13]. Additionally, mesopores have been shown to provide better dispersion of a metal component in comparison with conventional microporous systems [14–17].

Several preparative strategies have been developed to increase the accessibility of the active sites and various aspects of these efforts have been reviewed and highlighted during the last years [18–25]. Overall, mesopores in zeolites can be created during synthesis or in a post-synthesis modification step. The predominant approach for the creation of mesopores directly during synthesis is to apply templates such as carbon nanoparticles [26], however, many other templating approaches have been reported as well [24]. Aside from synthesizing mesoporous zeolites directly, mesopores can also be created post-synthetic by demetallating part of the zeolite for instance by steaming (dealumination), acid treatment (dealumination) or base treatment (desilication) [19,25]. Alkaline treatment of zeolites has received attention for many years [27,28], however, it was not until microscopy images and porosity data were reported [29,30] and the field was systematically investigated on ZSM-5 [31,32] that the potential of the approach was realized. Apart from ZSM-5 other mesoporous zeolites including mordenite [33] and beta [34] have been prepared by desilication using sodium hydroxide or sodium carbonate as the base. Recently, also organic bases such as tetraalkylammonium hydroxides, which are relatively expensive, have been used to generate mesoporosity [35,36]. The main practical benefit of using organic bases is that calcination of the treated material directly affords the zeolite in its acidic form,

---

[*] Corresponding author. Tel.: +45 2275 2000; fax: +45 4527 2999.
E-mail address: pabb@topsoe.dk (P. Beato).

[1] Present address: Lindoe Offshore Renewables Center, Kystvejen 100, DK-5330 Munkebo, Denmark.

0920-5861/$ – see front matter © 2011 Elsevier B.V. All rights reserved.
doi:10.1016/j.cattod.2011.03.045

Table 1
An overview of the base treatments with product yield, Si/Al ratio and textural properties of the parent and treated zeolites.

Sample name	Treatment[a]			Yield (%)	Textural properties				
	Base	C (mol/L)	t (h)		S_{BET} (m^2/g)	S_{micro}[b] (m^2/g)	S_{ext}[b] (m^2/g)	V_{micro}[b] (cm^3/g)	V_{meso}[c] (cm^3/g)
HZ(Pa)	–	–	–	–	347	200	146	0.10	0.13
HZ(0.3)NaOH(1)	NaOH	0.3	1.0	41	431	188	243	0.10	0.67
HZ(0.8)NaOH(1)	NaOH	0.8	1.0	11	274	102	172	0.05	0.56
HZ(0.3)GC(1)	Gua_2CO_3	0.3	1.0	97	355	207	148	0.10	0.15
HZ(0.8)GC(1)	Gua_2CO_3	0.8	1.0	97	348	213	135	0.11	0.13
HZ(1.5)GC(1)	Gua_2CO_3	1.5	1.0	97	349	210	139	0.11	0.13
HZ(0.6)GH(1)	GuaOH	0.6	1.0	97	347	207	139	0.11	0.13
HZ(1.6)GH(1)	GuaOH	1.6	1.0	95	343	207	136	0.11	0.13
HZ(3.0)GH(1)	GuaOH	3.0	1.0	92	348	208	140	0.11	0.13
HZ(0.8)GC(5.5)	Gua_2CO_3	0.8	5.5	93	363	218	145	0.11	0.15
HZ(1.6)GH(5.5)	GuaOH	1.6	5.5	85	384	221	163	0.12	0.20

[a] All preparations were carried out using 30 mL base/gram zeolite at 65 °C.
[b] t-plot method.
[c] V_{total} (N_2 uptake at $p/p_o = 0.99$) − V_{micro}.

whereas alkali metal based bases necessarily entails an additional ion-exchange step.

Herein we report an inexpensive method to produce mesoporous ZSM-5 using guanidinium hydroxide and compare the approach to samples treated with sodium hydroxide or guanidinium carbonate. The catalytic performances of the samples were explored in the MTG reaction as well as in SCR of NO_x with NH_3. These particular reactions were chosen because they are both of technical importance and the challenges are very different. In the MTG reaction, deactivation by coke-formation is the main challenge, whereas in SCR it is the dispersion of active iron species. The samples in this study were characterized using X-ray powder diffraction (XRPD), elemental analysis (ICP-OES), scanning electron microscopy (SEM), transmission electron microscopy (TEM), energy dispersive X-ray analysis (EDX), temperature-programmed desorption of ammonia (NH_3-TPD), Fourier transform infrared spectroscopy (FTIR) (with and without NO adsorbed on the samples), diffuse reflectance ultraviolet–visible spectroscopy (DRUV–VIS) and nitrogen physisorption measurements.

2. Experimental

2.1. Preparation of H-ZSM-5 zeolite

The synthesis of the conventional Na-ZSM-5 was adopted from the published procedure [37] and the following chemicals of reagent grade were used: sodium silicate (27.7% SiO_2, 8.2% Na_2O Borup Kemi), tetrapropylammonium bromide (98%, Aldrich), aluminum sulfate octadecahydrate (>98%, Sigma–Aldrich), sodium chloride (98%, Sigma–Aldrich) and deionized water. The composition of the zeolite gel was: SiO_2: 0.011 Al_2O_3: 0.05 TPA_2O: 0.66 Na_2O: 20 H_2O.

The resulting zeolite gel was transferred into a stainless steel autoclave and crystallized at 120 °C for 8 days. After the autoclave was cooled to room-temperature, the product was suspended in water, filtered by suction, re-suspended in water, and filtered again. This procedure was repeated four times. Then the product was dried at 110 °C for 10 h. The organic template was removed by controlled combustion in air in a muffle furnace at 550 °C for 18 h, and finally the sample was ion-exchanged twice with a 1.0 M solution of ammonium nitrate (1:20 mass ratio) and calcined again at 550 °C for 5 h.

2.2. Base treatments of H-ZSM-5

For each base treatment 15 g of zeolite was suspended in 450 mL of base solution and stirred for 1 h at 65 °C. The remaining zeolite was filtered by suction, washed with de-ionized water, dried and calcined at 550 °C for 5 h. All samples treated with sodium hydroxide were furthermore ion-exchanged and calcined using the ion-exchange procedure described in Section 2.1.

Guanidinium hydroxide was obtained by mixing solutions of calcium hydroxide with guanidinium carbonate in a molar ratio of 1:1.2 and stirred for 10 h. The obtained calcium carbonate was separated from the formed guanidinium hydroxide solution by filtration. All samples have been named according to HZ(x)y(z), where x, y and z are the concentration, identity of base and time of treatment respectively as given in Table 1.

2.3. Iron impregnation on base treated H-ZSM-5

Fe-containing HZSM-5 catalysts were prepared by impregnation of the base-treated H-form of the zeolite with an aqueous solution of iron nitrate with the aim of an iron loading of 4.5 wt%. For impregnation, the incipient wetness method was used. The impregnated samples were dried at 100 °C for 8 h followed by calcination at 550 °C for 5 h. Fe-containing samples have been named accordingly FeZ(x)y(z), where x, y and z are the concentration, identity of base and time of treatment, respectively.

2.4. Characterization

XRPD patterns were recorded on a Phillips PW1800 system in θ–2θ geometry working in reflectance mode using Cu Kα_1 radiation (λ = 1.541 Å).

Elemental composition of each sample was determined using inductively coupled plasma optical emission spectroscopy (ICP-OES) on acid digested samples using a Perkin Elmer Optima 7300 DV instrument.

SEM images were recorded on samples with deposited Pd/Pt for improved conductivity using a FEI Quanta 600 instrument.

For TEM images, the samples were crushed and dispersed in ethanol using ultrasound. A droplet was added to a Cu grid covered with a lacey C film and the grid was dried in air. Representative images of the zeolite were obtained at 200 kV on a Philips/FEI CM-200 electron microscope.

Nitrogen physisorption was performed at liquid nitrogen temperature using a Micromeritics ASAP 2020 instrument. All samples were outgassed in vacuum at 300 °C for 16 h prior to measurements.

NH_3-TPD was performed using 100 mg of sample (150–300 μm sieve fraction) loaded into a quartz tube reactor (i.d. 4 mm). Prior to NH_3 adsorption, the sample was treated for 2 h at 500 °C in a flow of dry nitrogen (100 N mL/min) in order to remove physically adsorbed water and other impurities. The sample was then saturated with ammonia (4000 ppm NH_3 in N_2, flow 100 N mL/min) at 150 °C for 1 h. After saturation with ammonia the sample was kept

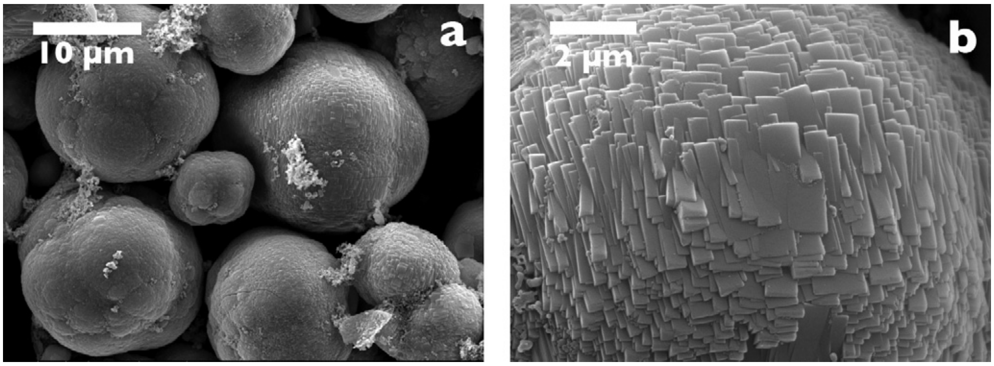

Fig. 1. Representative SEM micrograph of the parent H-ZSM-5 sample showing large particles, with an average size between 5 and 15 μm (a). SEM micrograph at a higher magnification of one particle showing many intergrowths (b).

in a N_2 flow for 4 h to remove weekly adsorbed ammonia. During the desorption step the temperature was ramped to 600 °C at 10°/min. The rate of NH_3 desorption was monitored by a CX4000 Gasmet FTIR gas analyzer.

DRUV–VIS spectra of the powdered Fe-containing samples were recorded at room temperature on dried samples (120 °C/12 h) using a Varian Cary 300 instrument in the 200–800 nm range. The baseline was recorded using a Spectralon® standard reference. The Fe-containing samples were diluted to 1 wt% in the ZSM-5-parent sample. Spectra were recorded in reflectance mode and converted into the Kubelka-Munk function $F(R)$. For all samples the $F(R)$ values were <2.

FTIR spectra were recorded on a Bio-Rad FTS 575C spectrometer equipped with a MCT detector. All samples were measured as self-supporting disks with a wafer density of ca. 10 mg/cm^2 in transmission mode (spectral resolution of 2 cm^{-1} over 256 scans). All spectra have been normalized to the pellet density. For activation and treatments with different probe molecules, the samples were mounted into a home-made, in situ IR cell [38] (KBr windows) connected to a vacuum/gas dosing apparatus and attached to a quartz reactor in which pre-treatment was carried out. Iron-free samples were activated at 450 °C under vacuum (~10^{-5} mbar) for 14 h, before cooling to 150 °C. Reference spectra and all following spectra were measured at 150 °C. Pyridine adsorption was carried out at 150 °C for 30 min at a partial pressure of 5–7 mbar, followed by desorption of excess pyridine into a cryo-vacuum (liq. N_2) for 30 min. The relative amounts of Lewis (L) and Brønsted (B) acid sites was determined after adsorption of pyridine from the integral band intensities at 1450 cm^{-1} (L) and at 1550 cm^{-1} (B) using extinction coefficients (ε) (L) = 2.22 cm/μmol, and ε (B) = 1.67 cm/μmol as reported in literature [39].

The pre-treatment of Fe-containing samples was carried out by heating (5°/min) the samples in 15% O_2/Ar (60 mL/min) from RT to 400 °C for 14 h and afterwards cooled to RT. Before dosing NO, the cell was evacuated at RT for 30 min (~10^{-5} mbar). NO adsorption was performed at RT by admitting 3–5 mbar NO into the cell. After 1 h of adsorption (intermediate spectra not shown), excess NO was removed carefully until no rotational contribution (gas phase) to the spectra was observed.

2.5. Catalytic testing

2.5.1. Methanol-to-gasoline catalytic test

The conversion of methanol into gasoline was performed in a 10-channel parallel steel reactor setup (i.d. 3.0 mm). Each reactor was loaded with 150 mg zeolite catalyst (150–300 μm sieve fraction) and one channel was left empty for feed analysis. Methanol (>99.9% Aldrich Chromasolv®) was fed to the reactor using a syringe pump (ISCO 500D, dual pump system) and evaporated in an argon stream. The methanol conversion was measured under the conditions: 350 °C, 15 bar (14.2% MeOH in Ar) using a total flow of 350 N mL/min. The reactor exit gas was monitored with an online GAM200 mass spectrometer connected via a channel selector valve (Valco, 10-position valve SC configuration). The individual reactor flows were measured and accounted for in the data analysis, which has been described in further detail elsewhere [40].

2.5.2. NH_3-SCR catalytic test

The selective catalytic reduction of NO by ammonia (NH_3-SCR) was carried out in a fixed bed quartz reactor (i.d. 4 mm). For each test 40 mg of catalyst, sieve fraction 150–300 μm, diluted with SiC to a total bed height of 14 mm, was loaded between two layers of inert quartz wool. The reactant gas composition used was 500 ppm NO, 530 ppm NH_3, 10% O_2, and 5% H_2O, balanced with N_2, and the total flow rate was maintained at 300 N mL/min. Prior to the activity measurements samples were treated in the reaction mixture for 1 h at 550 °C. The activity test was carried out by ramping down from 550 °C to 170 °C, at 2 °C/min. The outlet gas was analyzed by a Gasmet CX4000 FTIR analyzer.

3. Results and discussion

3.1. Characterization of the obtained materials

3.1.1. Synthesis and textural properties

The zeolite gel composition was chosen to produce large particles with many crystal intergrowths, because it has been suggested earlier that desilication by alkaline treatment proceeds via attack at intergrowth boundaries [41]. A Si/Al ratio of 40 was selected according to the optimum ratio of 25–50 for desilication by alkaline bases also reported in the literature [31,32,42]. The XRPD of the parent sample after combustion of the organic template confirmed phase-pure ZSM-5-type material. SEM micrographs of the parent H-ZSM-5 are given in Fig. 1a and b showing that the parent sample consists of large spherical particles with diameters between 5 and 15 μm (Fig. 1a). A minor fraction of very small particles is also observed. Higher magnification (Fig. 1b) reveals that the larger particles are made from the intergrowth of smaller zeolite crystals. SEM images of selected post-treated samples, which exhibit the typical sponge-like appearance of mesoporous zeolites, can be found in the supporting information (S1).

Table 1 summarizes the textural properties of the conventional ZSM-5 and the mesoporous materials obtained via the different base treatments, including the parameters and yields for each procedure. For the parent sample, HZ(Pa), the micropore volume and specific surface area are within the typical range for microporous ZSM-5. All samples treated with guanidinium bases for 1 h do not show significant differences while the 0.80 M NaOH treatment was

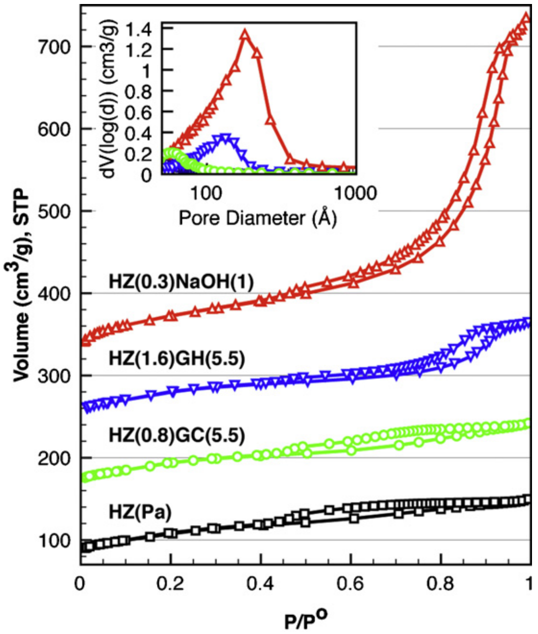

Fig. 2. Nitrogen physisorption isotherms together with the corresponding BJH pore size distribution from the desorption isotherm for selected samples showing the generation of mesopores.

apparently too severe, leading to a deterioration of the material as indicated by the decrease to half the original micropore volume and the loss of 89 wt% of material. These materials were excluded from further analysis. For the prolonged (5.5 h) guanidinium hydroxide and the 0.30 M NaOH treatment significant changes are evident from the N_2-physisorption data, indicating the formation of mesopores.

The N_2-physisorption isotherms and derived pore size distributions of these two samples are shown in Fig. 2 together with that of HZ(Pa) and HZ(0.8)GC(5.5). The isotherm from HZ(Pa) is typical for microporous material with a high nitrogen uptake at relative low pressures. Furthermore, a small uptake at intermediate pressures is noticed which is ascribed to the high surface roughness and intercrystalline voids. A similar uptake and a shallow hysteresis between 0.45 and 0.85 p/p_o is observed for HZ(0.8)GC(5.5), probably caused by the same effects. For the HZ(0.3)NaOH(1) and HZ(1.6)GH(5.5) samples a combined IUPAC type I and IV isotherm is seen with a clear hysteresis and uptake of nitrogen >0.4 p/p_o, which is typical for hierarchical materials with both micro- and mesoporosity. The BJH pore size distributions are centered around 170 Å and 130 Å for the sodium and guanidinium hydroxide treated samples, respectively. Smaller mesopore diameters in ZSM-5 samples have also been observed by Abello et al. [36] during desilication with tetraalkylammonium hydroxide bases compared to alkaline treatments. The difference was ascribed to the higher affinity of the organic cation to the zeolite surface resulting in slower desilication kinetics as well as a shielding effect towards OH^- attack by the organic cation.

The yields after the different base treatments agree well with the degree of mesoporosity and the severity of the treatment. This indicates that further mesoporosity might be generated for even longer treatments with guanidinium hydroxide.

Interestingly, the typical decrease in micropore volume, usually observed after desilication has not been observed in our materials. Instead, an increase to 0.11–0.12 cm^3/g for the longer guanidinium treatments was measured. An explanation may be given by taken into consideration that the parent sample contained minor amounts of very small crystallites (see Fig. 1), which is also reflected in the relatively large external surface area of the parent material. During base treatments the dissolution of smaller particles competes with the creation of mesopores. The two phenomena will have a compensating effect on the microporosity of the samples because the creation of mesopores typically occurs at the expense of microporosity, whereas the dissolution of smaller particles will oppositely lead to an increase in microporosity. The high surface to bulk ratio for the small particles eventually leads to the complete dissolution of them. If at the same time only a moderate mesopore formation takes place, a net increase in microporosity will be observed, which is the case for the guanidinium treated samples. If however dissolution of small particles occur together with the formation of extensive mesoporosity, as is the case for HZ(0.3)NaOH(1), both effects will compensate each other and no or only very moderate changes in microporosity will be observed.

Table 2
Overview of acidic properties for selected samples.

Sample	Si/Al[a]	NH_3-capacity[b]		N(B)/N(L)[c]
		μmol/g	Si/Al	
HZ(Pa)	34.9	214	77	2.0
HZ(0.3)NaOH(1.0)	17.6	327	64	1.0
HZ(0.8)GC(5.5)	34.7	236	70	1.8
HZ(1.6)GH(5.5)	32.0	256	69	1.9

[a] ICP-OES.
[b] NH_3-TPD (desorption at 150 °C), assuming $N_{NH3} = N_{Al}$.
[c] Ratio of Brønsted and Lewis acidity measured by Pyridine-FTIR.

Recently it was reported that a combined use of tetraalkylammonium hydroxides with sodium hydroxide leads to an optimal desilication procedure where mesoporosity is generated without compromising the microporosity [43]. Our results indicate that the behavior of the guanidinium cation is somewhat analogue to the tetraalkylammonium cation (seen by the smaller mesopore diameters and slower desilication kinetics) although the guanidinium cation is not a template for the zeolite structure. Therefore the combined use of guanidinium and sodium hydroxide should also lead to optimal desilication procedures with preservation of the microporosity.

3.1.2. *Acidic properties*

Table 2 summarizes the acidic properties for HZ(Pa), HZ(1.6)GH(5.5), HZ(0.8)GC(5.5) and HZ(0.3)NaOH(1) measured by elemental analysis, ammonia capacity and from infrared spectroscopy using pyridine as a probe molecule. Elemental analysis reveals a decrease in Si/Al ratio for the alkali treated sample as a consequence of the selective silicon leaching, while only a slight decrease is observed for both guanidinium treated samples confirming a less extensive silicon removal. The NH_3 capacity increases for all treated samples and is highest for HZ(0.3)NaOH(1). However, the large difference between Si/Al ratios from elemental composition and ammonia capacity can only be explained by the presence of weak- or non-acidic extra-framework aluminum (EFAL).

To further understand and quantify the different aluminum related sites in the materials, pyridine adsorption experiments have been performed and monitored via IR spectroscopy. The characteristic IR band of pyridine adsorbed on Brønsted acid sites (B) occurs at 1545 cm^{-1} and corresponds to the 19b vibration of the pyridinium ion, while pyridine adsorbed to a Lewis acid site (L) gives rise to a band at 1455 cm^{-1}. Taking into account the respective molar extinction coefficients, these bands have been used to determine the amount of EFAL by calculating the B/L ratio in the base treated samples (see Table 2 and Fig. 3). It should be noted that EFAL can occur as clustered species and therefore not all aluminum atoms are necessarily exposed to the surface. Consequently,

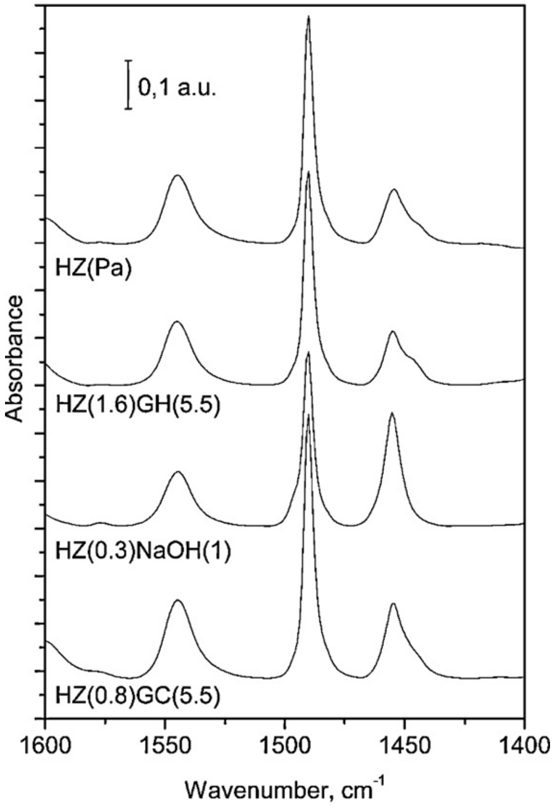

Fig. 3. FTIR spectra on selected H-ZSM-5 samples in the region of pyridine vibration.

the amount of Lewis acid sites does not automatically represent the amount of EFAL atoms. The B/L ratio of 2.0 for the HZ(Pa) sample indicates that a significant amount of the aluminum in the starting material is present as EFAL. A decrease in the B/L ratio, down to a value of one occurs for the alkali treated sample. This can only be rationalized by assuming that framework aluminum has been co-extracted during the desilication and converted to EFAL. In comparison the B/L ratio in guanidinium base treated samples decreases only slightly as a result of the reduced silicon removal and/or because realumination is less likely to occur due to the shielding effect from the guanidinium cation.

To check whether the removal of framework aluminum and the subsequent deposition as EFAL had any effects on the accessibility to the acid sites in the micropores, it is useful to consider the IR difference spectra before and after pyridine adsorption (Fig. 4). From the difference spectra it is evident that all bands related to acid sites are eroded, which means that they are accessible for pyridine and consequently for any other molecule of similar size.

3.2. Performance in the MTG reaction

A straight forward and reliable measure of the catalyst performance in MTG is to compare the conversion capacities. The capacity can be calculated by dividing the weight amount of methanol passed over the catalyst bed when conversion has decreased to 50% by the catalyst mass [40]. Fig. 5a shows the conversion curves of the samples as a function of grams of methanol passed over the catalyst bed. The conversion capacity decreases according to HZ(0.3)NaOH(1) > HZ(1.6)GH(5.5) > HZ(0.8)GC(5.5) > HZ(Pa), resulting in conversion capacities of 876, 527, 400 and 340 g_{MeOH}/g_{cat}, respectively.

Hence, the conversion capacity of the sodium hydroxide treated sample increases by a factor of 2.6 compared to the parent sample, which is consistent with previous reports on desilication and MTG lifetime [44]. For HZ(1.6)GH(5.5) the conversion capacity is increased by a factor of 1.6, while HZ(0.8)GC(5.5) converts 1.2 times more methanol compared to the parent sample. A plot of the external surface area versus conversion capacity is shown in Fig. 5b and suggests that the observed catalyst enhancement correlates with the generated mesoporosity during the base treatments. Deviations from the relation might be due to several factors such as internal defects [45] or other microstructural differences. It is worth mentioning that the higher acid site density in the samples after base treatments did not have a negative effect on the life-time. This is despite that earlier findings have shown that low Si/Al ratios lead to accelerated coking [44].

Table 3
Chemical composition and ammonia capacity for iron containing samples.

Sample name	Fe wt%[a]	Fe/Al[a]	NH_3-capacity[b]
FeZ(Pa)	4.40	1.85	0.20 mmol/g
FeZ(0.3)NaOH(1)	4.58	0.94	0.22 mmol/g
FeZ(0.8)GC(5.5)	4.44	1.81	0.17 mmol/g
FeZ(1.6)GH(5.5)	4.42	1.80	0.19 mmol/g

[a] ICP-OES.
[b] NH_3-TPD.

3.3. Iron loading on treated samples

3.3.1. Introduction of iron in the base treated H-ZSM-5 zeolites

The four selected samples were loaded with iron using a simple incipient wetness impregnation procedure aiming for 4.5 wt% Fe. This high amount of iron was chosen to study the potential improved dispersion of iron in the base treated materials. It has been reported earlier that hierarchical ZSM-5 is able to disperse significantly higher amounts of active iron species compared to purely microporous zeolites [17]. In Table 3 the chemical composition and ammonia capacity for the samples are reported.

The amount of iron is comparable for all samples, whereas the Fe/Al ratio varies slightly for the FeZ(0.3)NaOH(1) sample due to the extensive desilication treatment.

Representative TEM images of FeZ(Pa), FeZ(0.3)NaOH(1) and FeZ(1.6)GH(5.5) of the main sample morphologies are given in Fig. 6. TEM images were taken with the purpose of visualizing the porosity of the base treated samples and the distribution of iron. Due to the observed similarities between FeZ(Pa) and FeZ(0.8)GC(5.5) in TEM, FeZ(Pa) was chosen as representative for both samples. The micrographs clearly show the presence of mesopores for the two base treated samples. FeZ(1.6)GH(5.5) is composed of discrete mesopores with pore sizes in the range of approximately 10 nm which is in good agreement with the pore size distributions from the N_2-physisorption data. For FeZ(0.3)NaOH(1) the mesopores have developed into a sponge-type network, with a broader pore size distribution. In addition to the zeolite morphology, agglomerates of iron oxide particles with particle sizes in the range of 2–100 nm were observed for all samples as a consequence of the high iron load (not shown). However, the presence of highly dispersed iron species in the zeolites was confirmed by EDX measurements in zones where iron oxide agglomerates could not be visually observed (S2, supporting information). This heterogeneity between large iron agglomerates and highly dispersed iron species is further confirmed by spectroscopic methods, which are reported in the following section.

3.3.2. Iron speciation

NO adsorption on metal oxide surfaces is known to give rise to a range of species which can be distinguished with FTIR due to the sensitivity of the vibrations of these bonds to the metal valence state [46]. In this study, NO adsorption was used to probe the nature

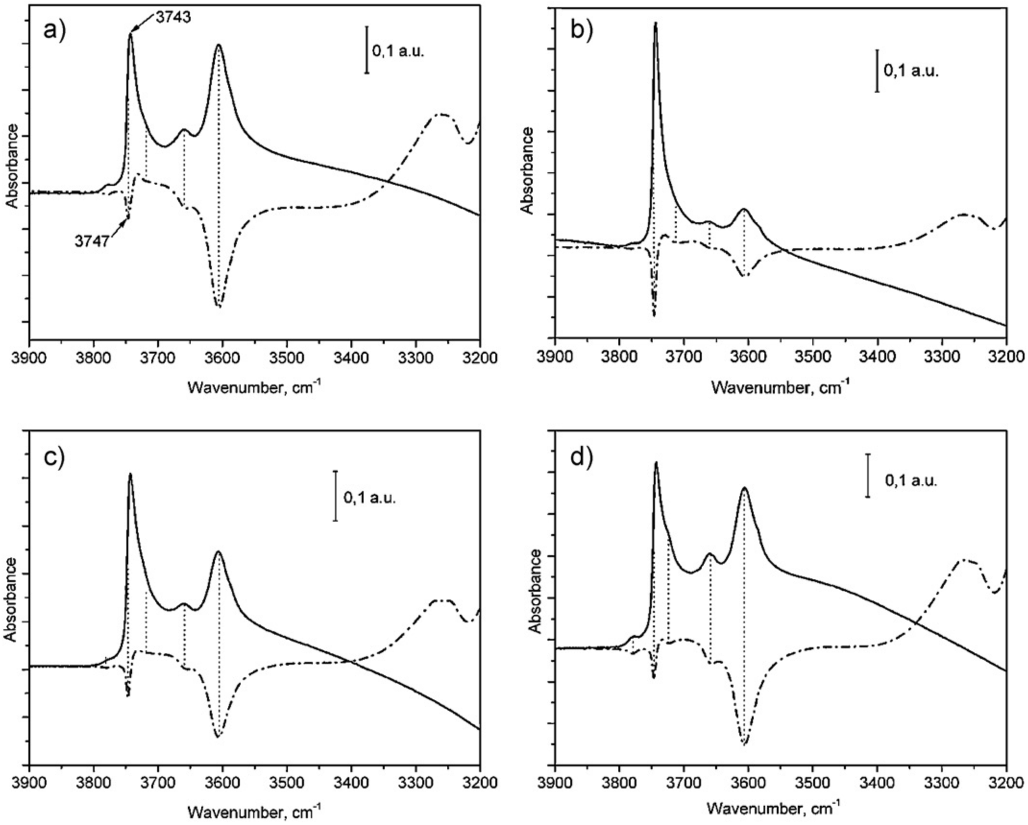

Fig. 4. FTIR spectra on selected H-ZSM-5 samples in the ν(OH region) corresponding to the spectra shown in Fig. 3. The spectra before pyridine adsorption are given in solid lines, while the difference spectra after pyridine adsorption is given in a dashed-dotted line. (a) HZ(Pa), (b) HZ(0.3)NaOH(1), (c) HZ(1.6)GH(5.5), (d) HZ(0.8)GC(5.5).

of surface metal sites after an oxidative pre-treatment (see Section 2.4). The use of oxidative conditions rather than a pre-treatment at high temperature in vacuum or inert gas, as usually applied, should give a more realistic picture of the involved metal sites in SCR, which under operating conditions will be exposed to high amounts of oxygen.

In Fig. 7 the NO adsorption spectra for the FeZ(Pa), FeZ(0.3)NaOH(1), FeZ(0.8)GC(5.5) and FeZ(1.6)GH(5.5) samples in the stretching vibration region of N–O are shown. The most dominant feature in the spectra is the band centered at 1877 cm^{-1} assigned to mononitrosyl complexes with Fe^{3+}-species [46]. The band is for all four samples very asymmetric confirming the heterogeneity of iron clusters and species in the samples. There is a clear increase in the band intensity in the order FeZ(Pa) < FeZ(1.6)GH(5.5) < FeZ(0.8)GC(5.5) < FeZ(0.3)NaOH(1) indicating a higher dispersion of the iron in the same order. All samples show two smaller bands at 1816 and 1919 cm^{-1} which are assigned to highly dispersed Fe^{2+} sites with two nitrosyl ligands, *e.g.* $Fe^{2+}(NO)_2$ [46]. However, a couple of bands at 1918 and 1810 cm^{-1} has also been assigned to highly dispersed $Fe^{2+}(NO)_3$ complexes [47]. Rivallan et al. recently discussed the nature of two different $Fe^{2+}(NO)_3$ complexes giving rise to the same couple of

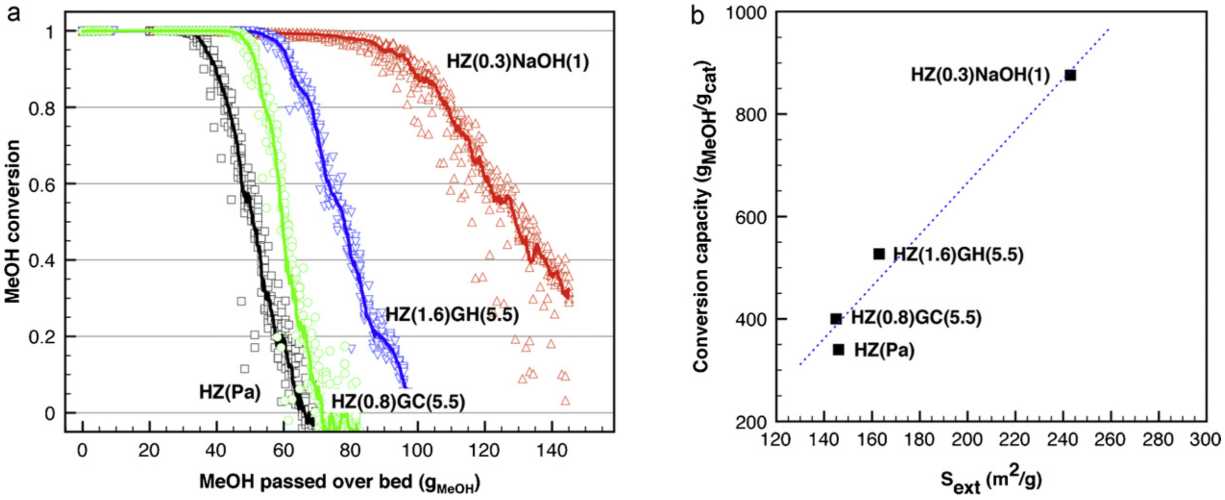

Fig. 5. Conversion of methanol per g_{MeOH} passed over the catalyst bed for selected samples (a). Conditions were 350 °C, p = 15 bar, total flow = 350 N mL/min in 10 reactors, 150 mg_{cat} ~ WHSV = 2.8 h^{-1}. Relation between mesopore surface area in m^2/g and conversion capacity in g_{MeOH}/g_{cat} (b).

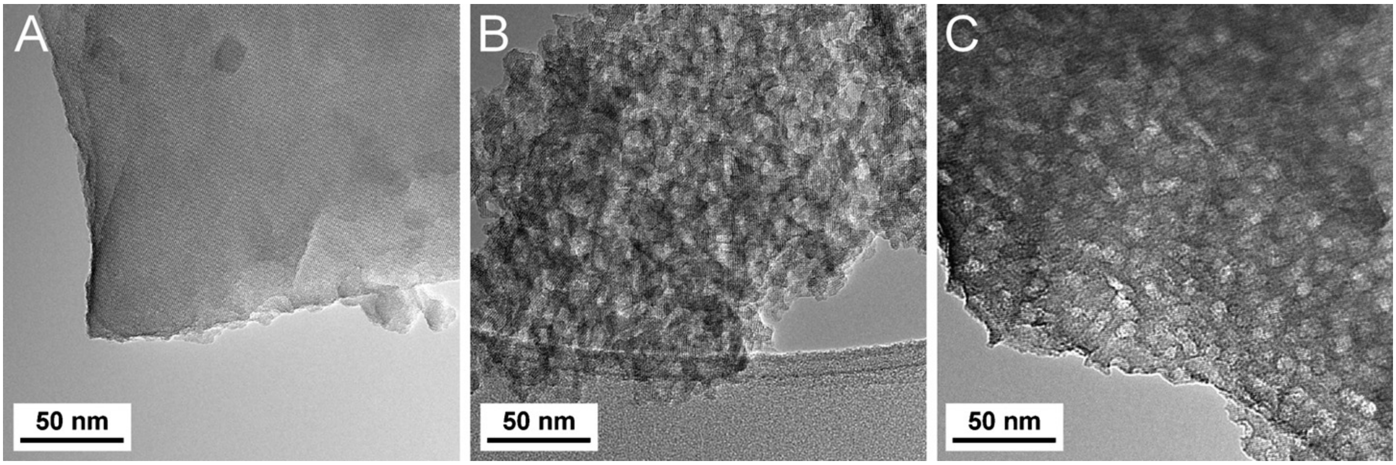

Fig. 6. Representative TEM micrographs of the iron loaded ZSM-5 zeolites in the three samples (A) FeZ(Pa), (B) FeZ(0.3)NaOH(1) and (C) FeZ(1.6)GH(5.5).

bands and named the related iron sites Fe_A and Fe_B. With decreasing NO partial pressure the complex formed at Fe_A is gradually transformed into $Fe^{2+}(NO)_2$ with a corresponding increase in the bands at 1845 and 1767 cm^{-1}. The fact that no bands for the di-nitrosylic complex appear upon removal of NO ligands from the $Fe^{2+}(NO)_3$ complex formed at Fe_B, has been explained by a ligand substitution of neighbouring SiOSi or SiOAl groups in the framework of the zeolite. Hence, Fe_B species should be located in different geometric positions as the Fe_A sites. It is important to mention that we have not observed the appearance of new bands upon decreasing the NO pressure for any of the samples (not shown). Regardless the exact assignment of the bands at 1919 and 1816 cm^{-1} it is clear that they represent highly dispersed Fe^{2+}-sites, and that the base treated samples contain a significantly higher amount.

All base treated samples furthermore show a medium intensity band at 2134 cm^{-1} together with a broad contribution ranging from 1650 to 1550 cm^{-1}, which are assigned to NO^+ and NO_3^- species, respectively. The parent sample shows only weak bands at these wavenumbers. The formation of these surface species has been explained by the disproportionation of N_2O_4 which is formed via oxidation of NO [47] and therefore represent relevant intermediates in the SCR reaction [48].

The optical properties of the Fe containing zeolites have also been investigated by DRUV–VIS spectroscopy on samples in air, diluted with the parent H-ZSM-5 sample (Fig. 8). Fe containing zeolites are generally characterized by complex strong absorptions in the UV–visible region, with ligand to metal charge transfer (LMCT) character, from the oxygen atoms to the iron sites. Very similar features are expected in case of tetrahedral or octahedral species, so the technique is not unequivocal in case of isolated species. Conversely, the frequency of LMCT bands are affected by the clustering and shifted towards higher wavelength with increasing nuclearity. The set of spectra in Fig. 8 show very similar features. All spectra are characterized by two main components. The first band has a maximum ranging from 375 to 400 nm, while the second is situated between 505 and 525 nm. Following the assignments in literature [49,50] we assign the bands to LMCT transitions in Fe_2O_3 clusters of increasing nuclearity. Note that the ratio between intensities of the two maxima is different in the four spectra. In particular,

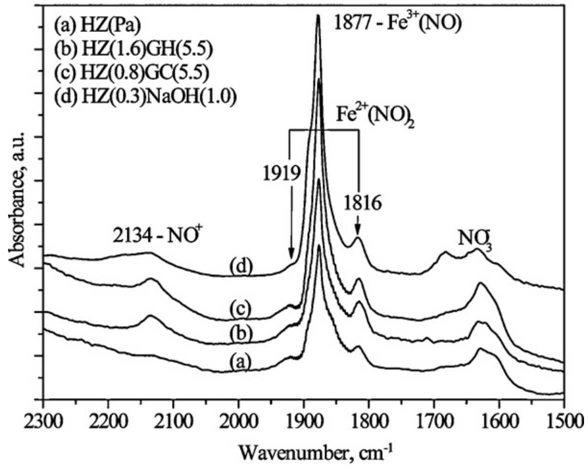

Fig. 7. FTIR spectra of NO adsorbed on selected iron containing ZSM-5 samples.

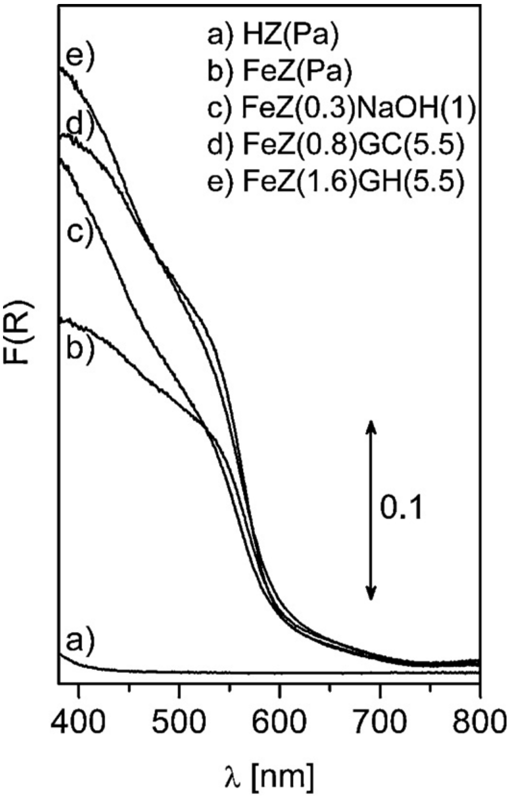

Fig. 8. DRUV–VIS spectra of selected iron containing ZSM-5 samples.

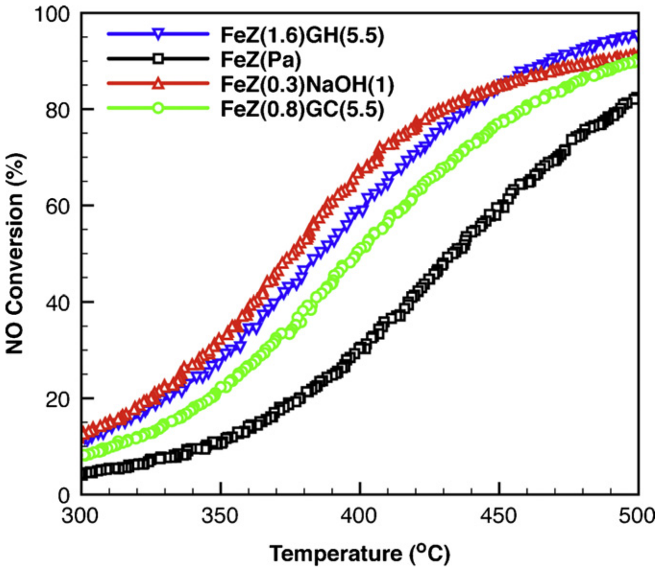

Fig. 9. NO conversion with NH_3 of zeolites loaded with iron as a function of temperature. Conditions used were: 500 ppm NO, 530 ppm NH_3, 10% O_2, 5% H_2O and N_2 balance (total flow 300 N mL/min), 40 mg catalyst (150–300 μm sieve fraction).

FeZ(Pa) shows two maxima with similar intensity. For the two samples treated with guanidinium bases, the component at lower wavelengths is more intense with respect to the second one and therefore suggests a higher abundance of smaller Fe_2O_3 clusters compared to the parent iron containing sample.

From the obtained spectra it is not possible to make any consideration about the presence of isolated sites as their spectroscopic features, if present, would have been covered by the much more intense absorption of clustered units. The UV–VIS results, though not clear without ambiguity, supplement the NO-FTIR data and lead to the picture of a higher amount of dispersed and most likely also oligomeric sites on the base treated samples compared to FeZ(Pa). Groen et al. have carried out alkaline treatments of ZSM-5 zeolites already containing iron [51,52]. In general they observe an increase in isolated iron species at the expense of oligomeric clusters upon base treatment. Although we have introduced iron after leaching, it demonstrates how base treatments lead to changes in iron speciation towards higher dispersion.

3.4. Iron zeolite performance in NH_3-SCR

Fig. 9 shows the NO conversion as a function of temperature in selective catalytic reduction of NO with NH_3 for the conventional and base treated samples loaded with iron.

The base treated samples outperform the parent sample at all temperatures in the same order as in the MTG reaction (*i.e.* FeZ(Pa) < FeZ(0.8)GC(5.5) < FeZ(1.6)GH(5.5) < FeZ(0.3)NaOH(1)). It has been reported that at lower temperatures monomeric iron species are active in SCR, whereas at higher temperatures also oligomeric species contribute to activity [53,54]. In this case spectroscopic results have shown that the base treated samples are able to accommodate a higher amount of dispersed Fe species compared to the conventional zeolite. The improved SCR activity observed over the base treated samples could therefore be explained by a better iron dispersion leading to a higher amount of active iron species in these samples. The sample with the highest degree of mesoporosity (FeZ(0.3)NaOH(1.0)) shows the lowest light off temperature. However, the sample prepared from guanidinium carbonate, which has no or low degree of mesoporosity, shows only a slightly higher light off temperature than the guanidinium hydroxide sample with some mesoporosity. A positive effect of the mesopores on the SCR activity could therefore be present, but the small differences in activity between the base treated samples indicate that the mesopores do not influence the catalyst performance in SCR to the same extent as for the MTG reaction. Instead, it appears that desilication influences the speciation of iron inside the zeolite.

Above 450 °C the observed NO conversion over FeZ(0.3)NaOH(1) is lower than over the FeZ(1.6)GH(5.5), due to a higher degree of ammonia oxidation, which again might be ascribed to the relative different amounts of iron species in each sample as deduced from DRUV–VIS and infrared spectroscopy.

4. Conclusions

A new base treatment procedure for ZSM-5 zeolite was introduced, which resulted in a hierarchical pore system using guanidinium hydroxide. The results of this treatment were compared to procedures involving guanidinium carbonate and the typically applied sodium hydroxide. In comparison to the sodium hydroxide treatment, the guanidinium hydroxide base treatment provokes only moderate leaching of Si from the framework for comparable treatment times. The data suggests that the mesoporosity can easily be further increased by longer treatment times.

In the methanol-to-gasoline reaction all base treatments lead to longer catalyst lifetimes. A good correlation between the conversion capacity and the mesoporosity of the samples was found despite the higher acid site density in the desilicated materials. The base treatments provoke a shift in the relative amounts of Brønsted and Lewis acidic sites, which was most drastically observed for the alkali treated sample.

Iron impregnated samples were tested in the selective catalytic reduction of NO with NH_3. Also for this reaction the mesoporosity was beneficial for the higher activity of the samples, but less pronounced than for MTG. On the basis of spectroscopic results, the improved NO conversion could be correlated to an increasing number of active Fe sites facilitated by the prior base treatment. Interestingly, the guanidinium base treated materials showed an enhanced selectivity towards NO reduction at higher temperatures.

The new desilication method represents a versatile alternative to the commonly applied alkali bases and may also be an attractive approach in industry as the mesopore generation does not require an additional ion-exchange step. Furthermore an optimal desilication procedure may be envisioned by the combined use of guanidinium and sodium hydroxide to generate mesoporosity without compromising microporosity.

Acknowledgements

The authors would like to thank Prof. Silvia Bordiga and Prof. Carlo Lamberti for the fruitful discussions on the spectroscopic part of the manuscript.

Appendix A. Supplementary data

Supplementary data associated with this article can be found, in the online version, at doi:10.1016/j.cattod.2011.03.045.

References

[1] A. Corma, Chem. Rev. 95 (1995) 559–614.
[2] F. Di Renzo, F. Fajula, Stud. Surf. Sci. Catal. 157 (2005) 1–12.
[3] C.E.A. Kirchhock, S.P.B. Kremer, J. Vermant, G. van Tendeloo, P.A. Jacobs, J.A. Martens, Chem. Eur. J. 11 (2005) 4306–4313.
[4] J.C. Groen, W. Zhu, S. Brouwer, S.J. Huyink, F. Kapteijn, J.A. Moulijn, J. Perez-Ramirez, J. Am. Chem. Soc. 129 (2007) 355–360.
[5] X. Wei, P.G. Smirniotis, Micropor. Mesopor. Mater. 97 (2006) 97–106.
[6] C.H. Christensen, K. Johannsen, E. Törnqvist, I. Schmidt, H. Topsøe, C.H. Christensen, Catal. Today 128 (2007) 117–122.

[7] M. Kustova, K. Egeblad, C.H. Christensen, A.L. Kustov, C.H. Christensen, Stud. Surf. Sci. Catal. 170 (2007) 267–275.
[8] C.H. Christensen, K. Johannsen, I. Schmidt, C.H. Christensen, J. Am. Chem. Soc. 125 (2003) 13370–13371.
[9] M. Kustova, P. Hasselriis, C.H. Christensen, Catal. Lett. 96 (2004) 205–211.
[10] M. Kustova, S.B. Rasmussen, A.L. Kustov, C.H. Christensen, Appl. Catal. B 67 (2006) 60–67.
[11] M. Kustova, M.S. Holm, C.H. Christensen, Y.-H. Pan, P. Beato, T.V.W. Janssens, F. Joensen, J. Nerlov, Stud. Surf. Sci. Catal. 174 (2008) 117–122.
[12] D.H. Choi, J.W. Park, J.H. Kim, Y. Sugi, Polym. Degrad. Stab. 91 (2006) 2860–2866.
[13] L. Zhao, B. Shen, J. Gao, C. Xu, J. Catal. 258 (2008) 228–234.
[14] C.H. Christensen, I. Schmidt, A. Carlsson, K. Johansen, K. Herbst, J. Am. Chem. Soc. 127 (2005) 8098–8102.
[15] I. Melian-Cabrera, S. Espinosa, J.C. Groen, B. Linden, F. Kapteijn, J.A. Moulijn, J. Catal. 238 (2006) 250–259.
[16] A.L. Kustov, T.W. Hansen, M. Kustova, C.H. Christensen, Appl. Catal. B 76 (2007) 311–319.
[17] A.L. Kustov, K. Egeblad, M. Kustova, T.W. Hansen, C.H. Christensen, Top. Catal. 45 (2007) 159–163.
[18] Y. Tao, H. Kanoh, L. Abrams, K. Kaneko, Chem. Rev. 106 (2006) 896–910.
[19] S. van Donk, A.H. Janssen, J.H. Bitter, K.P. de Jong, Catal. Rev. 45 (2003) 297–319.
[20] J. Cejka, S. Mintova, Catal. Rev. 49 (2007) 457–509.
[21] M. Hartmann, Angew. Chem. Int. Ed. 43 (2004) 5582–5880.
[22] L.V. Tosheva, P. Valtchev, C. R. Chimie 8 (2005) 475–484.
[23] F. Schüth, Annu. Rev. Mater. Res. 35 (2005) 209–238.
[24] K. Egeblad, C.H. Christensen, M. Kustova, C.H. Christensen, Chem. Mater. 20 (2008) 946–960.
[25] J. Perez-Ramirez, C.H. Christensen, K. Egeblad, C.H. Christensen, J.C. Groen, Chem. Soc. Rev. 37 (2008) 2530–2542.
[26] C.H. Jacobsen, C. Madsen, J. Houzvicka, I. Schmidt, A. Carlsson, J. Am. Chem. Soc. 122 (2000) 7116–7117.
[27] R.M. Dessau, E. Valyocsik, N.H. Goeke, Zeolites 12 (1992) 776–779.
[28] H. Lietz, K.H. Schnabel, C. Peuker, T. Gross, W. Storek, J. Völter, J. Catal. 148 (1994) 562–568.
[29] M. Ogura, S.Y. Shinomiya, J. Tateno, Y. Nara, E. Kikuchi, H. Matsukata, Chem. Lett. (2000) 882–883.
[30] M. Ogura, S.Y. Shinomiya, J. Tateno, Y. Nara, M. Nomura, E. Kikuchi, H. Matsukata, Appl. Catal. A 219 (2001) 33–43.
[31] J.C. Groen, J.A. Moulijn, J. Perez-Ramirez, J. Mater. Chem. 16 (2006) 2121–2131.
[32] J.C. Groen, L.A.A. Peffer, J.A. Moulijn, J. Perez-Ramirez, Chem. Eur. J. 11 (2005) 4983–4995.
[33] J.C. Groen, T. Sano, J.A. Moulijn, J. Perez-Ramirez, J. Catal. 251 (2007) 21–27.
[34] J.C. Groen, S. Abello, L. Villaescusa, J. Perez-Ramirez, Micropor. Mesopor. Mater. 114 (2008) 93–102.
[35] M.S. Holm, M.K. Hansen, C.H. Christensen, Eur. J. Inorg. Chem. (2009) 1194–1198.
[36] S. Abello, A. Bonilla, J. Perez-Ramirez, Appl. Catal. A 364 (2009) 191–198.
[37] N. J. Blom, US Patent 5151259.
[38] N.-Y. Topsøe, H. Topsøe, J. Catal. 75 (1982) 354–374.
[39] C.A. Emeis, J. Catal. 141 (1993) 347.
[40] T.V.W. Janssens, J. Catal. 264 (2009) 130–137.
[41] M.S. Holm, S. Svelle, F. Joensen, P. Beato, C.H. Christensen, S. Bordiga, M. Bjørgen, Appl. Catal. A 356 (2009) 23–30.
[42] J.C. Groen, L.A.A. Peffer, J.A. Moulijn, J. Pérez-Ramírez, J. Phys. Chem. B 108 (2004) 13062–13065.
[43] J. Pérez-Ramírez, D. Verboekend, A. Bonilla, S. Abelló, Adv. Funct. Mater. 19 (2009) 3972–3979.
[44] J. Kim, M. Choi, R. Ryoo, J. Catal. 269 (2010) 219–228.
[45] K. Barbera, F. Bonino, S. Bordiga, T.V.W. Janssens, P. Beato, J. Catal. (2011), in press, doi:10.1016/j.jcat.2011.03.016.
[46] K.I. Hadjiivanov, Catal. Rev. Sci. Eng. 42 (2000) 71–144.
[47] M. Rivallan, G. Ricchardi, S. Bordiga, A. Zcchina, J. Catal. 264 (2009) 104–116.
[48] S. Brandenberger, O. Kröcher, A. Tissler, R. Althoff, Catal. Rev. 50 (2008) 492–531.
[49] S. Bordiga, R. Buzzoni, F. Geobaldo, C. Lamberti, E. Giamello, A. Zecchina, G. Leofanti, Petrini, G. Tozzolo, G. Vlaic, J. Catal. 158 (1996) 486–501.
[50] J.M. Pérez-Ramírez, S. Kumar, A. Brückner, J. Catal. 223 (2004) 13–27.
[51] J.C. Groen, A. Brückner, E. Berrier, L. Maldonado, J.A. Moulijn, J. Pérez-Ramírez, J. Catal. 243 (2006) 212–216.
[52] J.C. Groen, L. Maldonado, E. Berrier, A. Brückner, J.A. Moulijn, J. Pérez-Ramírez, J. Phys. Chem. B 110 (2006) 20369–20378.
[53] M. Høj, M.J. Beier, J.-D. Grunwaldt, S. Dahl, Appl. Catal. B 93 (2009) 166–176.
[54] S. Brandenberger, O. Kröcher, A. Tissler, R. Althoff, Appl. Catal. B 95 (2010) 348–357.